

From Masks to Pixels and Meaning: A New Taxonomy, Benchmark, and Metrics for VLM Image Tampering

Xinyi Shang^{1,2,*}, Yi Tang^{1,*}, Jiacheng Cui^{1,*}, Ahmed Elhagry¹, Salwa K. Al Khatib¹, Sondos Mahmoud Bsharat¹, Jiacheng Liu¹, Xiaohan Zhao¹, Jing-Hao Xue², Hao Li¹, Salman Khan¹, Zhiqiang Shen^{1,†}

¹Mohamed bin Zayed University of Artificial Intelligence, ²University College London

*Equal Contribution, †Corresponding author

Existing tampering detection benchmarks largely rely on object masks, which severely misalign with the true edit signal: many pixels inside a mask are untouched or only trivially modified, while subtle yet consequential edits outside the mask are treated as natural. We reformulate VLM image tampering from coarse region labels to a pixel-grounded, meaning and language-aware task. First, we introduce a taxonomy spanning edit primitives (replace/remove/splice/inpaint/attribute/colorization, etc.) and their semantic class of tampered object, linking low-level changes to high-level understanding. Second, we release a new benchmark with per-pixel tamper maps and paired category supervision to evaluate detection and classification within a unified protocol. Third, we propose a training framework and evaluation metrics that quantify pixel-level correctness with localization to assess confidence or prediction on true edit intensity, and further measure tamper meaning understanding via semantics-aware classification and natural language descriptions for the predicted regions. We also re-evaluate the existing strong segmentation/localization baselines on recent strong tamper detectors and reveal substantial over- and under-scoring using mask-only metrics, and expose failure modes on micro-edits and off-mask changes. Our framework advances the field from masks to pixels, meanings and language descriptions, establishing a rigorous standard for tamper localization, semantic classification and description. Code and benchmark data are available at <https://github.com/VILA-Lab/PIXAR>.

Correspondence: Zhiqiang Shen (Zhiqiang.Shen@mbzuai.ac.ae)

1 Introduction

“ What is real? How do you define ‘real’? ”

— Morpheus, *The Matrix* (1999)

Advances in generative AI (Wu et al., 2025; Comanici et al., 2025a; Xia et al., 2024) have enabled the creation of photorealistic imagery, posing serious threats to digital media authenticity and trust (Xu et al., 2023; Pal et al., 2024; Monteith et al., 2024). Among these manipulations, fine-grained tampering (Gupta et al., 2025a; Guo et al., 2023; Nandi et al., 2023) is particularly insidious, as it subtly modifies partial regions of real images while remaining imperceptible to both human and conventional forensic methods (Guo et al., 2025; Huang et al., 2025). Consequently, developing robust detectors for fine-grained tampering is both a critical research challenge and a societal necessity.

Yet most established benchmarks still annotate “where the edit is” using coarse object masks, as summarized in Tab. 1. This practice implicitly assumes that edits are spatially confined to a pre-specified region and that all pixels within that region are equally manipulated. In practice, however, the edit signal is neither spatially nor metrically uniform: many pixels inside a mask remain unchanged or only trivially perturbed, while visually consequential adjustments (e.g., relighting halos, color bleeding, deblurring, seam removal) frequently extend outside the mask. As a result, mask-only evaluation conflates unedited pixels with true

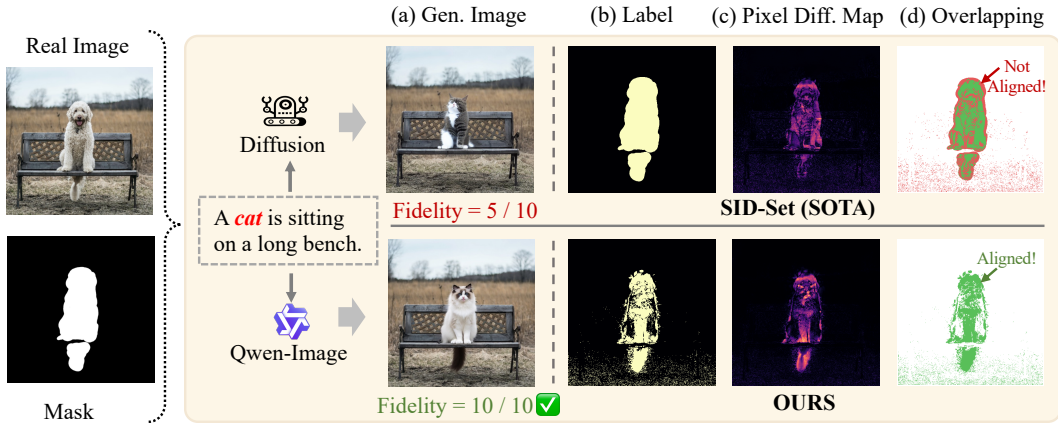


Figure 1 Pitfalls of Current Benchmarks and Our Remedy. (a) They contain unrealistic samples. (b)–(d) Their widely adopted mask-based label contains large regions of **not aligned** pixels with the true generative pixels. In contrast, our pixel label is precisely **aligned** with the true generative pixels.

tamper evidence and ignores off-mask artifacts, distorting both detector training and measurement.

We make this pixel-level real tamper explicit by contrasting per-pixel difference maps between original and tampered images (as shown in Fig. 1 (c)), and visualize prior weaker solution SID-Set (Huang et al., 2025)’s mask-defined labels in Fig. 1 (b). The visualization of Fig. 1 (d) reveals widespread misalignment (highlighted as **red points**) between the human-defined groundtruth and true pixel-level tamper, i.e., untouched pixels falsely labeled as “tampered” inside the mask and edited pixels incorrectly treated as “real” outside the mask. These label errors significantly penalize models for detecting genuine generative artifacts that fall beyond the mask boundary and, conversely, reward models that overfit to coarse shapes rather than the true edit footprint. Our analysis challenges the prevailing assumption that generative pipelines modify all masked pixels while preserving all unmasked areas, raising a fundamental question for the generative era: where, precisely, is the boundary between the “real” and the “generated”, and how should benchmarks encode that boundary?

To address this, we reformulate VLM image tampering as a **pixel-grounded**, meaning and text-**aware** task and construct a new benchmark called PIXAR. Concretely, we derive a difference map between the original and edited images and convert it into a binary supervision signal via a tunable threshold τ . The resulting label map \mathbf{M}_τ captures the spatial support of the edit at a controllable intensity level (Fig. 2): small τ emphasizes sensitivity to micro-edits, while larger τ emphasizes conservative, high-confidence changes. This thresholded construction decouples where an edit occurs (localization) from how strongly it manifests (intensity), enabling principled sweeps over τ to select operating points that best correlate with human judgments and downstream scenario use cases. Consequently, our formulation aligns evaluation with the physical tampering signal rather than proxy geometries.

Building on this reformulation, we introduce a large-scale benchmark – over 380K carefully curated training image pairs with rich, standardized metadata, and a well-balanced test set containing 40K image pairs with pixel-level and semantic-level labels. Each pair comprises a real source image, its tampered counterpart, the recommended binary pixel label \mathbf{M}_τ from a default τ , and the raw per-pixel difference map from which alternative labels for other τ values can be derived. To ensure manipulation diversity, our pipeline integrates eight editing strategies instantiated via state-of-the-art both open- and closed-source generative models, including Flux.2 (Labs, 2025), Gemini 2.5 (Comanici et al., 2025b), Gemini 3 (DeepMind, 2025), GPT-image-1.5 (OpenAI, 2026), Qwen-Image (Wu et al., 2025), Seedream 4.5 (Seedream et al., 2025). The strategies span replace/remove/splice/inpaint/attribute/colorization and related primitives, and we manually annotate the semantic class of the tampered target to connect low-level footprints to high-level semantics. Finally, we design a rigorous multi-stage filtering pipeline to guarantee the fidelity of tampered images and the precision of the corresponding labels. These designs yield a dataset that is simultaneously pixel-faithful and semantically structured, supporting detection, localization, and semantic understanding within a single protocol.

In summary, our contributions are threefold:

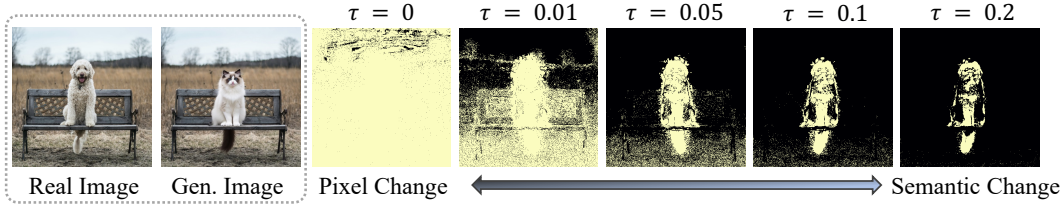


Figure 2 Visualization of our pixel-level label under different τ . Small τ emphasizes sensitivity to pixel edits, while larger τ emphasizes semantic changes.

1. We are the *first* to expose the core flaw of mask-based benchmarks, i.e. *misalignment with true generative edits*, and redefine tampering with pixel-level and semantic supervision to yield precise, faithful labels.
2. We build PIXAR, a large-scale, high-fidelity benchmark using state-of-the-art VLMs and human semantic label annotation, integrating 8 manipulation types with rigorous effectiveness and fidelity checks and accurate pixel annotations, establishing a principled foundation for the generative era.
3. We introduce a training framework and pixel-wise, realistic evaluation metrics, and extensively re-evaluate the state-of-the-art detectors on our PIXAR, revealing key limitations (e.g., micro- and off-mask failures) and setting stronger, more reliable baselines.

2 Related Work

Tampered Image Datasets. The rapid evolution of generative models, from Generative Adversarial Networks (GANs) (Zhu et al., 2017; Abdal et al., 2019; Xia et al., 2022) to diffusion models (Nichol et al., 2021; Croitoru et al., 2023; Yang et al., 2023; Rombach et al., 2022) and large Vision-Language Models (VLMs) (Zhang et al., 2024b; Comanici et al., 2025a; Wu et al., 2025), has necessitated the parallel development of robust and reliable detection benchmarks. Early benchmarks primarily focus on full-image generation (e.g., text-to-image), training detectors for binary real-versus-fake classification (Zhu et al., 2023; Zhong et al., 2023; Lu et al., 2023). However, as generative manipulations become increasingly subtle, recent research has shifted toward fine-grained tampering detection (Huang et al., 2025). Recently, SID-Set Huang et al. (2025) employs Stable Diffusion-based inpainting (Rombach et al., 2022) to construct a benchmark for tampering localization in social media images. Despite this progress, as summarized in Tab. 1, existing datasets largely rely on object masks as ground truth, leading to substantial misalignment with the true edit signal and fundamentally impairing detectors from learning true tampering footprints. In contrast, we redefine tampering with pixels, meanings, and language descriptions to yield precise, faithful supervision.

Tampered Image Detection. Tampering detection is commonly formulated as a classification task using CNN- or Transformer-based architectures (Nguyen et al., 2019; Chen et al., 2022). In addition, several studies Tan et al. (2024); Jeong et al. (2022) explore the frequency domain to capture generation-specific artifacts, while reconstruction-based methods such as RECCE (Cao et al., 2022) aim to improve feature

Table 1 Details of recent publicly available tampering benchmarks. The **Task** column indicates the evaluation type, where “B-Cla.” refers to binary classification (“real” vs. “tampered”), and “T-Loc.” denotes tampering localization. “Multi-Object” means multiple objects within one image can be tampered with.

Dataset	Year	Task	Multi-Object	Fidelity Check	Ground Truth
ArtiFact (Rahman et al., 2023)	2023	B-Cla.	✗	✗	-
TrainFors (Nandi et al., 2023)	2024	B-Cla. & T-Loc.	✗	✗	Mask
SIDBench (Schinas and Papadopoulos, 2024)	2024	B-Cla.	✗	✗	-
DiFF (Cheng et al., 2024)	2024	B-Cla.	✗	✗	-
M3Dsynth (Zingarini et al., 2024)	2024	B-Cla. & T-Loc.	✗	✗	Mask
SemiTruths (Pal et al., 2024)	2024	B-Cla. & T-Loc.	✗	✗	Mask
AI-Face (Lin et al., 2025)	2025	B-Cla.	✗	✗	-
SID-Set (Huang et al., 2025)	2025	B-Cla. & T-Loc.	✗	✗	Mask
PIXAR	2026	B-Cla. & T-Loc.	✓	✓	Pixel & Semantics

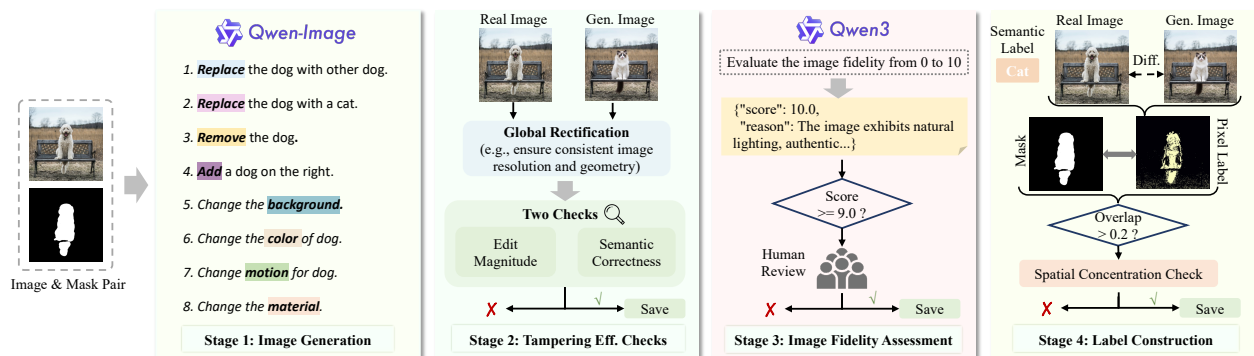


Figure 3 Overview of our PIXAR generation pipeline. The pipeline consists of four stages. *Stage 1: Image Generation:* We generate images with 8 tampering types. *Stage 2: Tampering Effectiveness Checks:* We filter out ineffective tampered images. *Stage 3: Image Fidelity Assessment:* The generated images are first assessed by Qwen3 (Yang et al., 2025) and then reviewed by human annotators. *Stage 4: Label Construction:* We manually annotate semantic labels and construct faithful pixel-level annotations.

robustness through reconstruction learning. Although these models achieve strong performance on images produced by seen generative models, their generalization to unseen ones remains limited. To mitigate this issue, CNNSpot Wang et al. (2020a) learns universal CNN artifacts, Fusing Ju et al. (2022) combines global and local representations through attention-based feature fusion, UnivFD Ojha et al. (2023) leverages the CLIP feature space for training-free real-fake discrimination, and LGrad Tan et al. (2023) maps images into gradient space to achieve model-driven generalization. More recently, Vision-Language Models have been introduced for tampering detection, such as SIDA (Huang et al., 2025), which fine-tunes LLaVA-based multimodal models, AntifakePrompt (Chang et al., 2023), which employs prompt tuning to improve detection accuracy and cross-model generalization, and FakeShield (Xu et al., 2024), which leverages VLM and a decoupled architecture to provide explainable detection and precise localization across diverse forgery domains, supported by the multi-modal MMTD-Set.

3 Benchmark Construction

To thoroughly train and evaluate image tampering detectors, we build PIXAR, a large-scale benchmark over 380K carefully curated training image pairs with rich, standardized metadata, and a well-balanced test set containing 40K image pairs with pixel-level and semantic-level labels. The design of PIXAR is guided by three principles: (i) **Diversity:** incorporating 8 tampering types that align well with real-world scenarios and demands; (ii) **Fidelity:** implementing rigorous fidelity checks to filter out low-fidelity samples; and (iii) **Precision:** ensuring precise labels for true tampering. Accordingly, we propose a four-stage generation pipeline, illustrated in Fig. 3. The following subsections detail each stage. Additional implementations and the construction of balanced test data are provided in App. B and App. C, respectively.

3.1 Image Generation

Data Source and Generative Models. We use real source images from the COCO (Lin et al., 2014), a large-scale benchmark with diverse scenes, objects, and contexts¹. For training set, we employ Qwen-Image VLMs (Wu et al., 2025) due to their significant advances in complex text rendering and precise image editing. For test set, we use both open- and closed-source generative models, including Flux.2 (Labs, 2025), Gemini 2.5 (Comanici et al., 2025b), Gemini 3 (DeepMind, 2025), GPT-image-1.5 (OpenAI, 2026), Qwen-Image (Wu et al., 2025), Seedream 4.5 (Seedream et al., 2025).

Diverse and Practical Tampering Types. Existing benchmarks mainly employ inter-class replacement for tampered image generation (Huang et al., 2025; Zingarini et al., 2024; Nandi et al., 2023), which fails to reflect the complexity of real-world manipulations. To align well with real-world tampered scenarios and

¹The project is stage-wise, and the images are continually expanded with more sources in our further versions.



Figure 5 Visualization of various tampering types in PIXAR. For each type, from top-left to bottom-right, the images show: original image with red shading indicating the modified object, tampered image, pixel-difference map overlaid on the tampered image, and our pixel-level label.

practical demands, we first analyzed large-scale Internet images to define 8 manipulation types (see Stage 1 of Fig. 3). Visual examples are shown in Fig. 5, and more details are provided in App. B.1.

Diverse Tampered Sizes and Complexities. To rigorously evaluate the robustness and discriminative performance of detection models across a spectrum of difficulty levels, we control two critical factors: *tampered size* and *tampered complexity*. Tampered size measures the extent of pixel-level modification, where smaller edits leave subtler traces and are thus harder to detect, while larger edits yield more significant artifacts. Tampered complexity reflects the compositional structure of manipulations. Beyond the conventional single-object edits (Tab. 1), we apply a multi-object, sequential protocol to better reflect iterative real-world forgeries. Visualizations and more implementation details are provided in App. B.1.

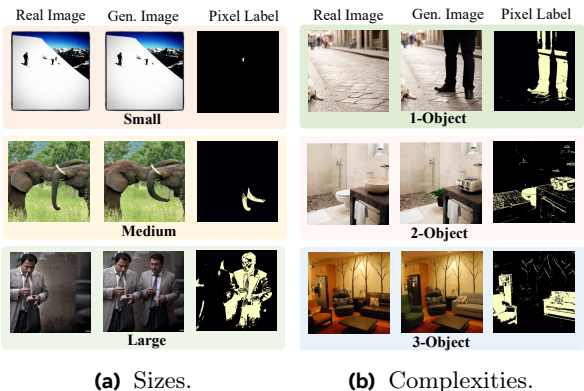


Figure 4 Visualization of tampered images with varying (a) tampered sizes and (b) tampered complexities.

3.2 Tampering Effectiveness Checks

Generative models frequently exhibit failure modes, such as unintended global repainting or trivial perturbations. Therefore, we implement a rigorous filtering pipeline (illustrated in Stage 2 of Fig. 3) to remove ineffective tampered images. The pipeline consists of two sequential steps: (1) *Global Rectification*, which enforces pixel-space consistency between the generated image and the original image, and (2) *Edit Magnitude and Semantic Correctness Checks*, which verify whether the resulting perturbations are both meaningful and aligned with the intended semantics.

Global Rectification. In practice, many contemporary generative models (e.g., Gemini) do not support a given target resolution, which may result in pixel-space misalignment between the generated image and the original image. Such geometric misalignment makes pixel-level difference maps unreliable, thereby corrupting the derived pixel labels \mathbf{M}_τ . To address this issue, we perform a geometric rectification step: we align I_{gen} to I_{orig} via feature matching, estimate a homography with RANSAC (Fischler and Bolles, 1981), and then recompute the difference map within this aligned coordinate pixel space. The qualitative comparison before and after global rectification is provided in Fig. 15 (a), verifying the efficacy of our rectification.

Edit Magnitude and Semantic Correctness Checks. After rectification, we rigorously evaluate whether the generative model successfully executed the requested edit for the original image. We observe three common failure cases: (i) *near-zero tampering*, where I_{gen} is almost identical to I_{orig} , yielding negligible signal in \mathbf{M}_τ ; (ii) *unintended global editing*, where large image regions are repainted beyond the target area, producing extensive noise in \mathbf{M}_τ ; and (iii) *unintended semantic edits*, where the visual change does not correspond to the text instruction. Accordingly, we assess validity from: (a) edit magnitude, to exclude trivial or overly global changes, and (b) semantic correctness, to ensure the visual manipulation matches the instruction. Visualization examples and implementation details are provided in App. B.2.

3.3 Image Fidelity Assessment

The reliability of the benchmark critically depends on the fidelity of its samples. Low-quality samples provide limited information for model training and evaluation (Zhang et al., 2024a; Gupta et al., 2025b). To ensure high fidelity of images, we design a rigorous image fidelity assessment process that combines automated evaluation by the state-of-the-art VLM Qwen3 (Yang et al., 2025) with human expert evaluation, as illustrated in Stage 3 of Fig. 3.

Automated VLM Assessment. Each tampered image candidate is first evaluated by Qwen3, which assigns a fidelity score from 0 to 10. Only tampered images achieving a score of ≥ 9 are shortlisted for subsequent human evaluation. This automated stage efficiently and effectively filters out low-fidelity images and thus improves the quality of our PIXAR.

Human Expert Review. Furthermore, we employ 10 human experts to manually review the generated images and remove those that appear unrealistic. Only samples that received a realism score of at least 4 out of 5 were retained. This human-in-the-loop evaluation ensures that subtle inconsistencies or semantic anomalies undetectable by automated models are effectively filtered out. We observe consistently high pass rates (90%) for intra-class replacement, splicing, inpainting, attribute modification, and colorization. In contrast, the inter-class replacement variant achieves a moderate pass rate of approximately 70%, while the removal type shows the lowest pass rate at around 55%. Representative examples of filtered and retained samples are provided in Fig. 16.

After the stringent image filtering process, we further validate quality by randomly sampling tampered images from SID-Set (Huang et al., 2025) and from our PIXAR for comparison, as shown in Fig. 6. Samples from SID-Set often appear visually unrealistic. In contrast, our dataset exhibits substantially higher fidelity, demonstrating a more reliable and principled foundation for tampered image detection.

3.4 Label Construction

To remedy the flaw of the existing mask-based label, we redefine tampering with pixel-level and semantic supervision. Consequently, detectors trained on our PIXAR learn not only *where* image tampering occurs (local pixel detection) but also *what* the tampered content means (semantic understanding).

Pixel Label. Given a pair of real and tampered images ($I_{\text{orig}}, I_{\text{gen}}$), we compute a difference map \mathbf{D} that quantifies the absolute pixel-wise discrepancy:

$$\mathbf{D}(\mathbf{x}, y) = |I_{\text{orig}}(\mathbf{x}, y) - I_{\text{gen}}(\mathbf{x}, y)|, \quad (1)$$

where (\mathbf{x}, y) indexes pixel coordinates. We then obtain a binary supervision mask \mathbf{M}_τ by thresholding \mathbf{D} with a tunable parameter τ :

$$\mathbf{M}_\tau(\mathbf{x}, y) = \mathbb{I}(\mathbf{D}(\mathbf{x}, y) > \tau), \quad (2)$$

where $\mathbb{I}(\cdot)$ denotes the indicator function. The resulting \mathbf{M}_τ captures the spatial support of the edit at a controllable intensity level: a small τ emphasizes sensitivity to micro-edits, while a larger τ emphasizes high-confidence modifications, as illustrated in Fig. 2. We provide more visualizations in Fig. 11 and a detailed analysis regarding the τ selection in Sec. 5.3.

Semantic Label. For each tampered object, we manually annotate its corresponding semantic class label (e.g., “cat” for the tampered image) and record this information as metadata associated with the image. Formally, let \mathcal{C} be the set of object classes that may be tampered, with multi-label ground truth $\mathbf{y} \in \{0, 1\}^{|\mathcal{C}|}$, where $y_c = 1$ if class c contains a tampered instance.

Label Reliability Checks. Finally, we validate the reliability of the pixel-level label with respect to semantic supervision. In practice, low-quality pixel labels arise from two issues: (i) *pixel-semantic inconsistency*, where the pixel change fails to reflect a valid semantic edit; and (ii) *poor spatial structure*, where the pixel label is

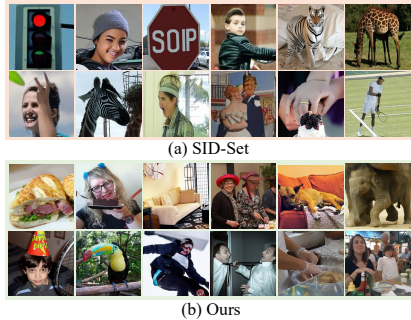


Figure 6 Comparison of fidelity between SID-Set and our PIXAR.

semantically consistent yet overly dispersed (often dominated by background pixels), making it unreliable for supervision. We address these failures using two checks:

(1) *Pixel-semantic consistency.* As shown in Fig. 7, in some cases, replacing an object (e.g., the black oven in the first row) with a visually similar one may yield negligible L_1 differences due to near-identical color and texture. Consequently, the pixel-level label underestimates the true semantic change, causing a pixel-semantic mismatch. To ensure faithful pixel supervision, we compute the overlap ratio between tampered pixels and the input mask, and discard samples with overlap < 0.2 . More examples and a detailed discussion of this threshold are provided in App. B.4.

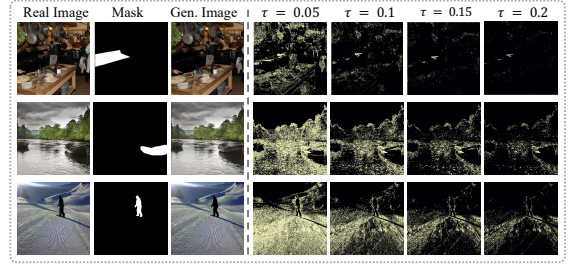


Figure 7 Examples of pixel-semantic inconsistency.

(2) *Spatial concentration.* Even when the semantic edit is correct, generation artifacts may introduce widespread background speckles, producing pixel labels that are scattered rather than object-shaped. Examples are visualized in Fig. 15 (c). Such dispersed labels are semantically consistent but structurally uninformative. To remove them, we quantify the spatial concentration of \mathbf{M}_τ using: (i) a grid-based concentration ratio, defined as the fraction of grid cells required to cover 80% of tampered pixels; and (ii) a local density score, defined as the median density of tampered pixels within a small neighborhood. Based on these metrics, we discard *Diverse* samples and retain only *Concentrated* pixel labels that provide clean, structured supervision. By filtering both inconsistent and dispersed cases, we obtain pixel supervision that is faithful to the edit and spatially well-formed.

3.5 Metadata

Each entry in our PIXAR benchmark encompasses four images accompanied by rich, standard metadata, providing comprehensive information about every stage of the tampering process, as illustrated in Fig. 8.

Specifically, each quadruple consists of: (i) a real source image, (ii) its tampered counterpart, (iii) the raw per-pixel difference map from which alternative labels for other τ values can be derived, and (iv) the recommended binary pixel-level label map \mathbf{M}_τ from a default τ . The accompanying metadata records detailed information on image generation, fidelity assessment process, and label construction. Notably, we provide text of detailed manipulation description as presented in App. B.5. Moreover, at the semantic level, beyond the semantic label, each tampered image is also accompanied by quantitative indicators such as the tampered size.

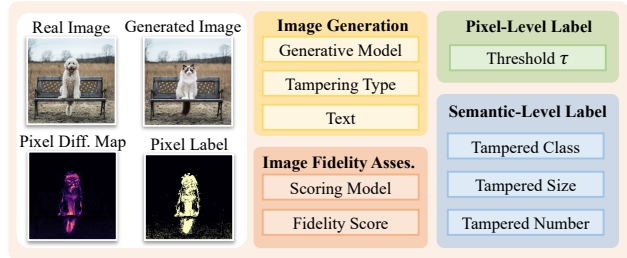


Figure 8 Composition of PIXAR. Each entry includes four images with detailed metadata.

4 Training Framework

Our tamper detector f_θ produces (i) a per-pixel tamper logit map $\mathbf{S} \in \mathbb{R}^{H \times W}$ and probabilities $\widehat{\mathbf{M}} = \sigma(\mathbf{S})$, and (ii) a multi-label semantic logit vector $\mathbf{z} \in \mathbb{R}^{|\mathcal{C}|}$ with $\hat{\mathbf{y}} = \sigma(\mathbf{z})$. Here $\sigma(\cdot)$ is the element-wise sigmoid, also a global vector for real or tamper detection. (iii) a natural language description detailing the specific tampering artifacts. Fig. 9 illustrates our training framework, \mathbf{h} represents the hidden feature vectors for different heads. We define the following losses:

Multi-label semantic loss. Because one or multiple objects can be tampered in one image, we train with a sigmoid cross-entropy (per class):

$$\mathcal{L}_{\text{sem}} = -\frac{1}{|\mathcal{C}|} \sum_{c \in \mathcal{C}} [y_c \log \hat{y}_c + (1 - y_c) \log (1 - \hat{y}_c)], \quad (3)$$

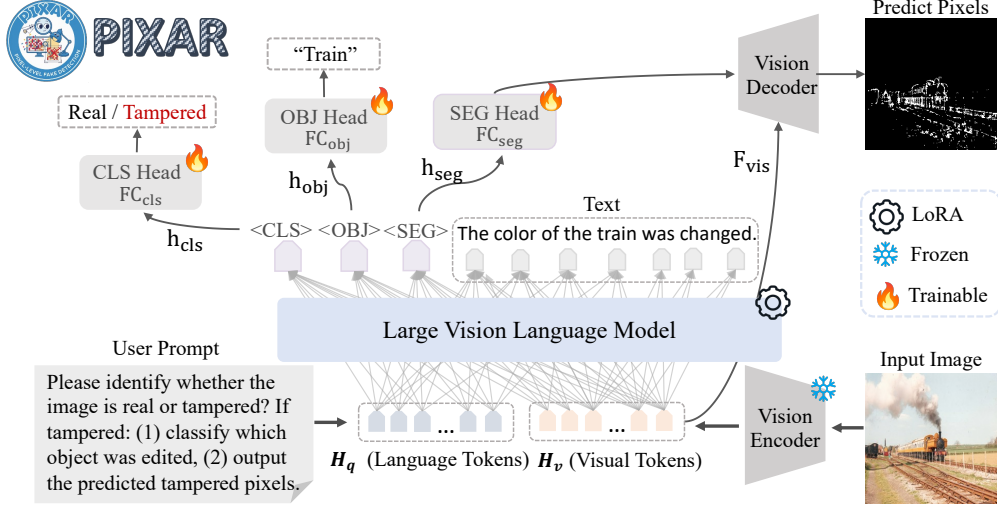


Figure 9 Overview of training framework.

where $y_c \in \{0, 1\}$ denotes the ground-truth for class c , and \hat{y}_c denotes the predicted probability for tampered area semantic label.

Pixel-wise BCE loss. We supervise the localization head with pixel-wise binary cross-entropy against our thresholded label \mathbf{M}_τ :

$$\mathcal{L}_{\text{bce}} = -\frac{1}{HW} \sum_{i,j} [\mathbf{M}_\tau(i,j) \log \widehat{\mathbf{M}}_{ij} + (1 - \mathbf{M}_\tau(i,j)) \log(1 - \widehat{\mathbf{M}}_{ij})], \quad (4)$$

where H, W are the height and width of an image.

Pixel-level DICE loss. Additionally, to further improve the localization of tampered pixels, we compute the DICE score (Azad et al., 2023) over connected-component masks. During training, we replace this surrogate mask with our pixel-level label \mathbf{M}_τ to more accurately reflect the true editing footprint:

$$\mathcal{L}_{\text{dice}} = 1 - \frac{2 \sum_{i,j} \widehat{\mathbf{M}}_{ij} \mathbf{M}_\tau(i,j) + \varepsilon}{\sum_{i,j} \widehat{\mathbf{M}}_{ij} + \sum_{i,j} \mathbf{M}_\tau(i,j) + \varepsilon}, \quad (5)$$

with a small $\varepsilon > 0$ for numerical stability.

Global image-level detection loss. To decide whether an image is real or tampered², we use a global detection head driven by a special token $\langle \text{CLS} \rangle$. Let the backbone produce the last hidden states $\mathbf{H}^{\text{hid}} \in \mathbb{R}^{N \times d}$, we extract the $\langle \text{CLS} \rangle$ representation $h_{\text{cls}} = \mathbf{H}^{\text{hid}}[\text{CLS}] \in \mathbb{R}^d$, and feed it to a detection head F_{cls} to obtain global class logits and probabilities:

$$\mathbf{u} = F_{\text{cls}}(h_{\text{cls}}) \in \mathbb{R}^2, \quad \hat{\mathbf{p}} = \text{softmax}(\mathbf{u}), \quad (6)$$

$$\mathcal{L}_{\text{cls}} = \mathcal{L}_{\text{CE}}(\hat{\mathbf{p}}, \mathbf{d}),$$

where \mathcal{L}_{cls} is the global detection loss, and $\mathbf{d} \in \{0, 1\}^2$ is the one-hot ground truth over {real, tampered}.

Tamper description generation loss. To provide a human-readable explanation of the manipulation, we generate a natural language description characterizing the tampered content (e.g., “A banana was added to the image.”). We use a multimodal causal language model conditioned on the input image and the textual prompt to model the autoregressive likelihood of the target token sequence $T^* = (t_1^*, \dots, t_L^*)$:

$$p_\phi(T^* | \mathbf{I}, P) = \prod_{i=1}^L p_\phi(t_i^* | t_{<i}^*, \mathbf{I}, P), \quad \mathcal{L}_{\text{text}} = -\sum_{i=1}^L \log p_\phi(t_i^* | t_{<i}^*, \mathbf{I}, P), \quad (7)$$

²We do not consider the fully synthetic category used in SIDA as it is a special case when all pixels are tampered. This case is already covered by our pixel-level detection, which is distinct from mask-based training.

Table 2 Pixel-level Tampered Region Localization Results and Associated Semantic Prediction Accuracy. PIXAR-Lite models are fine-tuned on a subset of our training data that contains masks to guide the generation of tampered images. In this setting, LISA and SIDA utilize these masks as ground-truth, whereas our model is supervised by the pixel-difference map with a threshold of $\tau = 0.05$. All methods use the same backbone model, either LISA-7B or LISA-13B as specified.

Methods	Semantic Classification		Pixel Localization				
	Top-1 Acc	Top-5 Acc	Recall	F1-Score	AUC	g-IoU	IoU
LISA-7B (Lai et al., 2024)	27.1	71.6	10.0	15.4	55.0	7.7	8.3
SIDA-7B (Huang et al., 2025)	27.1	71.9	15.0	21.1	55.0	10.7	11.8
PIXAR-7B-Lite (Ours)	28.2	75.0	26.4	26.1	55.2	14.3	15.0
PIXAR-7B (Ours)	36.2	77.0	29.8	30.6	62.2	16.1	18.1
LISA-13B (Lai et al., 2024)	30.6	75.1	11.4	17.3	55.6	9.0	9.5
SIDA-13B (Huang et al., 2025)	30.8	75.4	13.2	19.5	55.6	10.7	10.8
PIXAR-13B-Lite (Ours)	30.9	76.0	26.2	26.7	55.7	15.0	15.4
PIXAR-13B (Ours)	37.4	76.0	33.6	32.3	62.2	17.8	19.3

where $\mathcal{L}_{\text{text}}$ is the standard language modeling loss and P is the input prompt.

Final objective. Our training objective is to minimize a weighted combination of the five losses:

$$\mathcal{L}_{\text{total}} = \lambda_{\text{sem}}\mathcal{L}_{\text{sem}} + \lambda_{\text{bce}}\mathcal{L}_{\text{bce}} + \lambda_{\text{dice}}\mathcal{L}_{\text{dice}} + \lambda_{\text{text}}\mathcal{L}_{\text{text}} + \lambda_{\text{cls}}\mathcal{L}_{\text{cls}}. \quad (8)$$

where $\lambda_{\text{sem}}, \lambda_{\text{bce}}, \lambda_{\text{dice}}, \lambda_{\text{text}}, \lambda_{\text{cls}} > 0$ control the trade-offs between semantic understanding and pixel-accurate localization. We follow SIDA to choose values for λ_{bce} and λ_{cls} , and conduct ablations to determine the optimal value of λ_{sem} , λ_{dice} , and λ_{text} in Sec. 5.3. Unless stated otherwise, we use $\tau = 0.05$ to form \mathbf{M}_{τ} ; sweeping τ at training or validation time provides a principled knob to balance micro-edit sensitivity against conservative high-precision localization. More analysis for τ selection is provided in Sec. 5.3.

5 Experiments

Extensive experiments are performed to demonstrate the efficacy of our training framework and the redefined ground truth. We also benchmark the performance of various state-of-the-art detectors on the challenging PIXAR test set to provide a rigorous comparative analysis.

5.1 Experimental Setup

Training and Test Dataset Details. For both the training and test datasets, we set the threshold to $\tau = 0.05$ by default, with results of other τ discussed in Tab. 6. To ensure a fair evaluation of detector performance, the test dataset is carefully constructed to maintain a balanced distribution across tampered classes, tampered types, and tampered sizes, resulting in 40K images with their pixel-level and semantic-level labels. The detailed procedure for constructing the test set is provided in App. C.

Implementation Details. Leveraging SIDA (Huang et al., 2025) and LISA (Lai et al., 2024), our model is fine-tuned on PIXAR to transition from coarse to precise pixel-level localization. Through joint supervision via spatial, multi-label semantic (Eq. 3), and text generation (Eq. 7) losses, the framework simultaneously produces refined tamper masks, categorizes affected objects, and generates descriptive explanations.

Pixel-level and Semantic Metrics. To evaluate our framework and redefined ground truth, we introduce a novel paradigm integrating pixel-level localization with semantic classification. Moving beyond conventional binary or coarse region-level metrics, this approach enables a holistic assessment of fine-grained precision and the interpretive understanding of tampered artifacts. We assess pixel-level localization using Recall, F1-Score, and AUC to evaluate the precision of delineated tampered regions. To rigorously measure spatial overlap, we employ image-level mean IoU (g-IoU) for per-sample robustness and dataset-level IoU (IoU) for overall pixel-wise accuracy. Furthermore, semantic alignment is quantified via Top-1 and Top-5 Accuracy, evaluating the model’s proficiency in categorizing manipulated objects. By integrating spatial precision with semantic alignment, this interpretable framework provides a holistic benchmark for fine-grained image forensics.

Table 4 Comparison of existing deepfake detection methods and our models evaluated on the PIXAR test set.

Detector	Backbone	Data Distribution		Precision			Recall			F1-Score		
		GANs	Diffusion	Real	Fake	Overall	Real	Fake	Overall	Real	Fake	Overall
CnnSpot (Wang et al., 2020b)	ResNet-50 (He et al., 2016)	✓	✗	15.2	84.4	49.8	99.4	0.6	50.0	26.4	1.2	13.8
AntifakePrompt (Chang et al., 2023)	InstructBLIP (Dai et al., 2023)	✓	✓	4.6	84.8	44.7	0.01	99.9	50.0	0.03	91.7	45.9
SIDA-7B (Huang et al., 2025)	LISA-7B (Lai et al., 2024)	✗	✓	15.8	86.7	51.3	88.2	13.6	50.9	26.8	23.4	25.1
SIDA-13B (Huang et al., 2025)	LISA-13B (Lai et al., 2024)	✗	✓	16.5	86.3	51.4	62.0	42.8	52.4	26.0	57.2	41.6
PIXAR-7B	SIDA-7B (Huang et al., 2025)	✗	✓	39.1	97.6	68.4	89.9	74.9	82.4	54.5	84.8	69.7
PIXAR-13B	SIDA-13B (Huang et al., 2025)	✗	✓	33.6	98.4	66.0	93.4	66.7	80.1	49.5	79.5	64.5

Table 5 Comparison of detection performance across different generative sources.

Methods	Semantic Classification		Pixel Localization				
	Top-1 Acc	Top-5 Acc	Recall	F1-Score	AUC	g-IoU	IoU
GPT-Image-1.5 (OpenAI, 2026)	26.0	70.5	16.5	20.9	52.3	11.3	11.7
Seedream 4.5 (Seedream et al., 2025)	29.9	73.1	27.8	26.8	57.8	13.9	15.5
Gemini 3 (DeepMind, 2025)	33.8	75.7	34.5	26.7	67.0	14.6	15.4
Gemini 2.5 (Comanici et al., 2025b)	34.0	76.9	23.7	29.5	70.2	16.1	17.3
Flux.2 (Labs, 2025)	37.1	79.7	25.7	31.3	56.3	16.7	18.6
Qwen-Image (Wu et al., 2025)	52.0	84.0	56.5	41.6	76.6	22.6	26.3

5.2 Evaluation on PIXAR

Semantic Alignment and Localization Results. Tab. 2 reports the detection performance on the PIXAR test set. We select LISA and the SOTA method SIDA (Huang et al., 2025) as baselines for comparison. The results show that replacing coarse masks with our pixel-level labels simultaneously improves the model’s ability to accurately localize tampered regions and its semantic consistency in predicting the manipulation context. Notably, by merely refining the supervision signal, PIXAR-7B-Lite significantly outperforms SIDA-7B, elevating IoU from 6.9% to 14.9% and Top-1 Acc from 10.6% to 29.5%. This performance is further bolstered in PIXAR-7B, which achieves an additional 3.2% gain when scaled to the full training set. Tab. 3 further benchmarks our approach against FakeShield (Xu et al., 2024), where PIXAR demonstrates a commanding lead across all evaluated metrics. Most notably, PIXAR-7B achieves a near-doubling of localization accuracy, elevating the IoU from 9.3% to 18.1%. Collectively, these findings corroborate the effectiveness of accurate pixel-level supervision in achieving high-precision localization and the robustness of our framework across various evaluation settings.

Table 3 Performance comparison between PIXAR and FakeShield.

Methods	Pixel Localization				
	Recall	F1-Score	AUC	g-IoU	IoU
FakeShield	10.7	17.0	52.0	8.4	9.3
PIXAR-7B	29.8	30.6	62.2	16.1	18.1
PIXAR-13B	33.6	32.3	62.2	17.8	19.3

Binary Classification Performance. We evaluate a range of open-source deepfake detectors, CnnSpot (Wang et al., 2020a), AntifakePrompt (Chang et al., 2023), and SIDA-7B/13B (Huang et al., 2025) against our PIXAR models. As shown in Tab. 4, our models consistently outperform all baselines, highlighting their superior generalization, precise pixel-level localization, and robust binary classification.

Evaluation across Generative Models. To evaluate the cross-framework generalization of PIXAR, we present its performance across diverse generative paradigms in Tab. 5. Among them, GPT-Image-1.5 (OpenAI, 2026) is the most challenging case, with only 11.7% IoU and 26.0% Top-1 accuracy, whereas Qwen-generated images are the easiest to detect. We attribute this gap to domain shift, since the training data is primarily generated by Qwen-based. Despite this out-of-distribution (OOD) setting, PIXAR still exhibits robust and consistent detection performance across generations from all unseen frameworks, demonstrating that it captures universal artifacts that generalize beyond specific generative backbones and architectural designs.

5.3 Ablation Study

Influence of Different τ . To investigate the impact of training threshold τ on tampered-pixel localization, we conduct an ablation study in Tab. 6 while fixing the evaluation threshold at $\tau = 0.05$. Results show that increasing the training τ consistently hampers performance. As visualized in Fig. 2, a higher threshold filters

Table 6 Fixed Eval: Varying τ_{train} , fixed $\tau_{\text{eval}} = 0.05$.

	Semantic Class.		Pixel Localization				
	Top-1	Top-5	Recall	F1	AUC	g-IoU	IoU
$\tau = 0.05$	36.2	77.0	29.8	30.6	62.2	16.1	18.1
$\tau = 0.1$	35.2	76.1	15.4	22.4	60.9	13.1	12.6
$\tau = 0.2$	34.2	75.9	9.6	16.0	61.2	9.5	8.7

Table 7 Symmetric setting ($\tau_{\text{train}} = \tau_{\text{eval}}$).

	Semantic Class.		Pixel Localization				
	Top-1	Top-5	Recall	F1	AUC	g-IoU	IoU
PIXAR-7B ($\tau = 0.05$)	36.2	77.0	29.8	30.6	62.2	16.1	18.1
PIXAR-7B ($\tau = 0.1$)	34.6	75.9	17.4	23.5	61.4	10.6	12.0

out fine-grained pixel details, leaving only coarse semantic cues from the initial generation masks. This results in a less discriminative supervision signal for precise localization. To decouple the threshold’s intrinsic impact from the training-test discrepancy, we evaluate a consistent setting where identical τ values are used for both phases (Tab. 7). The results show that a lower τ consistently yields superior performance, validating that $\tau = 0.05$ provides a more discriminative and robust supervision signal for effective learning.

Influence of λ_{sem} . Tab. 8 explores the impact of semantic loss weight λ_{sem} . While pixel-level localization performance remains consistently robust across different weights, we observe that both lower (0.1) and higher (1.0) values of λ_{sem} lead to a marginal decline in Top-1 accuracy. This suggests that $\lambda_{sem} = 0.5$ strikes the optimal balance, providing sufficient semantic supervision without overshadowing other task objectives. We therefore adopt $\lambda_{sem} = 0.5$ to ensure maximum multi-task synergy.

Influence of λ_{text} . Tab. 9 investigates the trade-off controlled by λ_{text} . While a lower λ_{text} leads to suboptimal text generation, an excessively high value (e.g., $\lambda_{text} = 4.0$) tends to degrade semantic accuracy. We observe that $\lambda_{text} = 3.0$ strikes an optimal balance, delivering superior text quality without compromising core detection performance;

Table 8 Impact of Semantic Loss Weight.

	Semantic Classification		Pixel Localization				
	Top-1 Acc	Top-5 Acc	Recall	F1-Score	AUC	g-IoU	IoU
$\lambda_{sem} = 0.1$	35.1	76.2	29.7	30.3	62.2	15.9	17.9
$\lambda_{sem} = 0.5$	36.2	77.0	29.8	30.6	62.2	16.1	18.1
$\lambda_{sem} = 1.0$	35.2	76.2	29.7	30.5	62.0	16.0	18.0

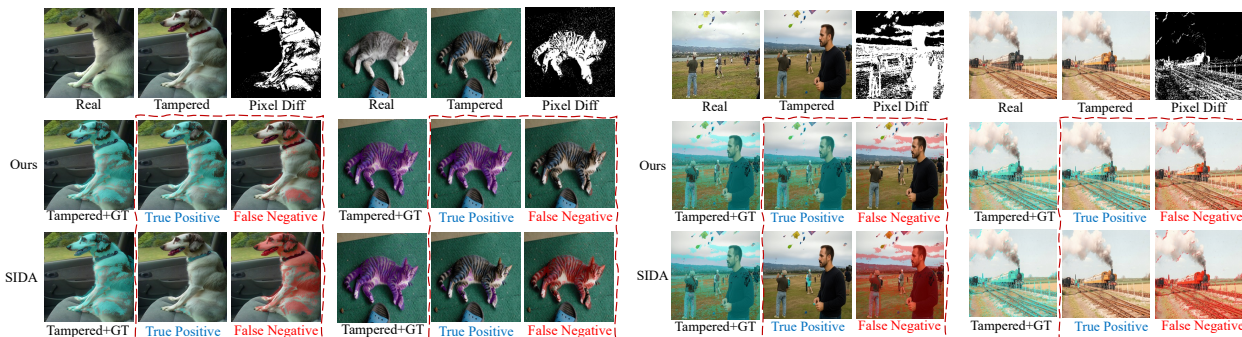
Table 9 Impact of Text Loss Weight.

	Semantic Classification		Pixel Localization		Text Quality
	Top-1 Acc	Top-5 Acc	g-IoU	IoU	Css
$\lambda_{text} = 2.0$	35.6	76.7	16.1	18.1	0.51
$\lambda_{text} = 3.0$	36.2	77.0	16.1	18.1	0.75
$\lambda_{text} = 4.0$	35.9	76.9	16.1	18.1	0.75

Influence of λ_{dice} . As summarized in Tab. 10, we conduct an ablation study to evaluate the contribution of Dice loss. The results demonstrate that incorporating λ_{dice} simultaneously enhances localization precision and semantic classification accuracy. This indicates that Dice loss provides superior spatial supervision, which refines mask boundaries and strengthens discriminative feature extraction.

Table 10 Impact of Dice Loss Weight λ_{dice} .

	Semantic Classification		Pixel Localization				
	Top-1 Acc	Top-5 Acc	Recall	F1-Score	AUC	g-IoU	IoU
$\lambda_{dice} = 0.0$	35.3	76.3	12.9	19.5	61.6	7.4	10.8
$\lambda_{dice} = 0.5$	36.0	76.6	22.8	27.3	62.0	13.5	15.8
$\lambda_{dice} = 1.0$	36.2	77.0	29.8	30.6	62.2	16.1	18.1

**Figure 10** Visualization comparison of prediction results between PIXAR and SIDA (Huang et al., 2025). The red dashed boxes show different prediction focuses compared to SIDA.

5.4 Analysis

Visualization. To visually compare the prediction results between PIXAR and SIDA (after fine-tuning on our dataset), we provide a visualization in Fig. 10. Within these red dashed boxes, we illustrate both true positives and false positives. For true positives, the closer the predicted tampered pixels are to the actual pixel differences, the better. False negatives refer to tampered pixels that the model fails to detect - the fewer, the better. The figure clearly demonstrates that *using masks as supervision fails to effectively recover the actual tampered regions*, most of the manipulated areas are missed (see the **false negatives** of SIDA), and only a small portion of the tampered regions are correctly detected. In contrast, our model exhibits a strong ability to accurately localize the tampered regions, with only a limited number of false negatives, further validating the effectiveness of the pixel-difference map over the ambiguous mask-based supervision in localization.

User study. To complement our quantitative metrics, we conducted a user study to evaluate the perceptual quality of tampered images in PIXAR. A random subset of our dataset was selected for this study, consisting of 1,000 images in total, including 500 real and 500 tampered samples. 10 participants were asked to perform two tasks: (1) classify whether the image is real or tampered, and (2) if tampered, localize the manipulated regions by drawing bounding boxes around the perceived alterations. As shown in Tab. 11, participants exhibited *low performance* in both binary classification and fine-grained localization, indicating that the tampered images in our dataset achieve high visual realism.

Table 11 Results of user study.

	Binary Classification			Localization		
	Precision	Recall	F1-Score	Recall	F1-Score	IOU
Human	22.2	55.5	31.0	17.4	18.8	10.7

6 Conclusion

In this work, we revisited VLM tampering as a pixel-grounded, meaning and language-aware task by deriving per-pixel difference maps and thresholding with τ to obtain controllable labels \mathbf{M}_τ . We also release PIXAR, a high-fidelity, large-scale benchmark of more than 420K image pairs built with 8 diverse manipulations, providing original and tampered images, rich metadata, raw difference maps, recommended \mathbf{M}_τ , and language descriptions for flexible supervision. We further introduced a pixel-aware training framework for localization with semantics-aware classification and natural language descriptions, and showed that state-of-the-art detectors are ill-scored under mask-only protocols, especially on micro-edits and off-mask changes, establishing a more realistic and reliable standard for fine-grained tamper detection and understanding.

Acknowledgements

This work is supported by the United AI Saqer Group Grant.

References

- Rameen Abdal, Yipeng Qin, and Peter Wonka. Image2stylegan: How to embed images into the stylegan latent space? In *ICCV*, pages 4432–4441, 2019.
- Luc Anselin. Local indicators of spatial association—lisa. *Geographical analysis*, 27(2):93–115, 1995.
- Reza Azad, Moein Heidary, Kadir Yilmaz, Michael Hüttemann, Sanaz Karimijafarbigloo, Yuli Wu, Anke Schmeink, and Dorit Merhof. Loss functions in the era of semantic segmentation: A survey and outlook. *arXiv preprint arXiv:2312.05391*, 2023.
- Junyi Cao, Chao Ma, Taiping Yao, Shen Chen, Shouhong Ding, and Xiaokang Yang. End-to-end reconstruction-classification learning for face forgery detection. In *CVPR*, pages 4113–4122, 2022.
- You-Ming Chang, Chen Yeh, Wei-Chen Chiu, and Ning Yu. Antifakeprompt: Prompt-tuned vision-language models are fake image detectors. *arXiv preprint arXiv:2310.17419*, 2023.
- Liang Chen, Yong Zhang, Yibing Song, Lingqiao Liu, and Jue Wang. Self-supervised learning of adversarial example: Towards good generalizations for deepfake detection. In *CVPR*, pages 18710–18719, 2022.

- Harry Cheng, Yangyang Guo, Tianyi Wang, Liqiang Nie, and Mohan Kankanhalli. Diffusion facial forgery detection. In *ACM MM*, pages 5939–5948, 2024.
- Gheorghe Comanici, Eric Bieber, Mike Schaekermann, Ice Pasupat, Noveen Sachdeva, Inderjit Dhillon, Marcel Blistein, Ori Ram, Dan Zhang, Evan Rosen, et al. Gemini 2.5: Pushing the frontier with advanced reasoning, multimodality, long context, and next generation agentic capabilities. *arXiv preprint arXiv:2507.06261*, 2025a.
- Gheorghe Comanici, Eric Bieber, Mike Schaekermann, et al. Gemini 2.5: Pushing the frontier with advanced reasoning, multimodality, long context, and next generation agentic capabilities. *arXiv preprint arXiv:2507.06261*, 2025b.
- Florinel-Alin Croitoru, Vlad Hondru, Radu Tudor Ionescu, and Mubarak Shah. Diffusion models in vision: A survey. *IEEE transactions on pattern analysis and machine intelligence*, 45(9):10850–10869, 2023.
- Wenliang Dai, Junnan Li, Dongxu Li, Anthony Tiong, Junqi Zhao, Weisheng Wang, Boyang Li, Pascale N Fung, and Steven Hoi. Instructblip: Towards general-purpose vision-language models with instruction tuning. *NeurIPS*, 36: 49250–49267, 2023.
- Google DeepMind. Gemini 3. 2025. Published November 2025.
- Martin A Fischler and Robert C Bolles. Random sample consensus: a paradigm for model fitting with applications to image analysis and automated cartography. *Communications of the ACM*, 24(6):381–395, 1981.
- Xiao Guo, Xiaohong Liu, Zhiyuan Ren, Steven Grosz, Iacopo Masi, and Xiaoming Liu. Hierarchical fine-grained image forgery detection and localization. In *CVPR*, pages 3155–3165, 2023.
- Xiao Guo, Xiaohong Liu, Iacopo Masi, and Xiaoming Liu. Language-guided hierarchical fine-grained image forgery detection and localization. *International Journal of Computer Vision*, 133(5):2670–2691, 2025.
- Parul Gupta, Shreya Ghosh, Tom Gedeon, Thanh-Toan Do, and Abhinav Dhall. Multiverse through deepfakes: The multifakeverse dataset of person-centric visual and conceptual manipulations. *arXiv preprint arXiv:2506.00868*, 2025a.
- Vipul Gupta, Candace Ross, David Pantoja, Rebecca J Passonneau, Megan Ung, and Adina Williams. Improving model evaluation using smart filtering of benchmark datasets. In *NAACL*, pages 4595–4615, 2025b.
- Kaiming He, Xiangyu Zhang, Shaoqing Ren, and Jian Sun. Deep residual learning for image recognition. In *CVPR*, pages 770–778, 2016.
- Zhenglin Huang, Jinwei Hu, Xiangtai Li, Yiwei He, Xingyu Zhao, Bei Peng, Baoyuan Wu, Xiaowei Huang, and Guangliang Cheng. Sida: Social media image deepfake detection, localization and explanation with large multimodal model. In *CVPR*, pages 28831–28841, 2025.
- Yonghyun Jeong, Doyeon Kim, Youngmin Ro, and Jongwon Choi. FrepGAN: robust deepfake detection using frequency-level perturbations. In *AAAI*, volume 36, pages 1060–1068, 2022.
- Yan Ju, Shan Jia, Lipeng Ke, Hongfei Xue, Koki Nagano, and Siwei Lyu. Fusing global and local features for generalized ai-synthesized image detection. In *ICIP*, pages 3465–3469. IEEE, 2022.
- Black Forest Labs. FLUX.2: Frontier Visual Intelligence. 2025. Accessed 2026-02-27.
- Xin Lai, Zhuotao Tian, Yukang Chen, Yanwei Li, Yuhui Yuan, Shu Liu, and Jiaya Jia. Lisa: Reasoning segmentation via large language model. In *CVPR*, pages 9579–9589, 2024.
- Li Lin, Santosh Santosh, Mingyang Wu, Xin Wang, and Shu Hu. Ai-face: A million-scale demographically annotated ai-generated face dataset and fairness benchmark. In *CVPR*, pages 3503–3515, 2025.
- Tsung-Yi Lin, Michael Maire, Serge Belongie, James Hays, Pietro Perona, Deva Ramanan, Piotr Dollár, and C Lawrence Zitnick. Microsoft coco: Common objects in context. In *ECCV*, pages 740–755, 2014.
- Zeyu Lu, Di Huang, Lei Bai, Jingjing Qu, Chengyue Wu, Xihui Liu, and Wanli Ouyang. Seeing is not always believing: Benchmarking human and model perception of ai-generated images. volume 36, pages 25435–25447, 2023.
- Scott Monteith, Tasha Glenn, John R Geddes, Peter C Whybrow, Eric Achtyes, and Michael Bauer. Artificial intelligence and increasing misinformation. *The British Journal of Psychiatry*, 224(2):33–35, 2024.
- Soumyaroop Nandi, Prem Natarajan, and Wael Abd-Almageed. Trainfors: A large benchmark training dataset for image manipulation detection and localization. In *ICCV*, pages 403–414, 2023.
- Huy H Nguyen, Junichi Yamagishi, and Isao Echizen. Capsule-forensics: Using capsule networks to detect forged images and videos. In *ICASSP*, pages 2307–2311, 2019.

- Alex Nichol, Prafulla Dhariwal, Aditya Ramesh, Pranav Shyam, Pamela Mishkin, Bob McGrew, Ilya Sutskever, and Mark Chen. Glide: Towards photorealistic image generation and editing with text-guided diffusion models. *arXiv preprint arXiv:2112.10741*, 2021.
- Utkarsh Ojha, Yuheng Li, and Yong Jae Lee. Towards universal fake image detectors that generalize across generative models. In *CVPR*, pages 24480–24489, 2023.
- OpenAI. Gpt image 1.5. 2026.
- Anisha Pal, Julia Kruk, Mansi Phute, Manogna Bhattaram, Diyi Yang, Duen Horng Chau, and Judy Hoffman. Semi-truths: A large-scale dataset of ai-augmented images for evaluating robustness of ai-generated image detectors. *NeurIPS*, 37:118025–118051, 2024.
- Gan Pei, Jiangning Zhang, Menghan Hu, Zhenyu Zhang, Chengjie Wang, Yunsheng Wu, Guangtao Zhai, Jian Yang, Chunhua Shen, and Dacheng Tao. Deepfake generation and detection: A benchmark and survey. *arXiv preprint arXiv:2403.17881*, 2024.
- Md Awsafur Rahman, Bishmoy Paul, Najibul Haque Sarker, Zaber Ibn Abdul Hakim, and Shaikh Anowarul Fattah. Artifact: A large-scale dataset with artificial and factual images for generalizable and robust synthetic image detection. In *ICIP*, pages 2200–2204, 2023.
- Robin Rombach, Andreas Blattmann, Dominik Lorenz, Patrick Esser, and Björn Ommer. High-resolution image synthesis with latent diffusion models. In *CVPR*, pages 10684–10695, 2022.
- Ethan Rublee, Vincent Rabaud, Kurt Konolige, and Gary Bradski. Orb: An efficient alternative to sift or surf. In *2011 International conference on computer vision*, pages 2564–2571. Ieee, 2011.
- Manos Schinas and Symeon Papadopoulos. Sidbench: A python framework for reliably assessing synthetic image detection methods. In *Proceedings of the 3rd ACM International Workshop on Multimedia AI against Disinformation*, pages 55–64, 2024.
- Team Seedream, Yunpeng Chen, Yu Gao, et al. Seedream 4.0: Toward next-generation multimodal image generation. *arXiv preprint arXiv:2509.20427*, 2025.
- Chuangchuang Tan, Yao Zhao, Shikui Wei, Guanghua Gu, and Yunchao Wei. Learning on gradients: Generalized artifacts representation for gan-generated images detection. In *CVPR*, pages 12105–12114, 2023.
- Chuangchuang Tan, Yao Zhao, Shikui Wei, Guanghua Gu, Ping Liu, and Yunchao Wei. Frequency-aware deepfake detection: Improving generalizability through frequency space domain learning. In *AAAI*, volume 38, pages 5052–5060, 2024.
- Hannes Taubenbock, Michael Wurm, Christian Geiss, Stefan Dech, and Stefan Siedentop. Urbanization between compactness and dispersion: Designing a spatial model for measuring 2d binary settlement landscape configurations. *International Journal of Digital Earth*, 12(6):679–698, 2019.
- Sheng-Yu Wang, Oliver Wang, Richard Zhang, Andrew Owens, and Alexei A Efros. Cnn-generated images are surprisingly easy to spot... for now. In *CVPR*, pages 8695–8704, 2020a.
- Sheng-Yu Wang, Oliver Wang, Richard Zhang, Andrew Owens, and Alexei A Efros. Cnn-generated images are surprisingly easy to spot... for now. In *CVPR*, pages 8695–8704, 2020b.
- Chenfei Wu, Jiahao Li, Jingren Zhou, Junyang Lin, Kaiyuan Gao, Kun Yan, Sheng-ming Yin, Shuai Bai, Xiao Xu, Yilei Chen, et al. Qwen-image technical report. *arXiv preprint arXiv:2508.02324*, 2025.
- Weihaio Xia, Yulun Zhang, Yujiu Yang, Jing-Hao Xue, Bolei Zhou, and Ming-Hsuan Yang. Gan inversion: A survey. *IEEE transactions on pattern analysis and machine intelligence*, 45(3):3121–3138, 2022.
- Zhuofan Xia, Dongchen Han, Yizeng Han, Xuran Pan, Shiji Song, and Gao Huang. Gsva: Generalized segmentation via multimodal large language models. In *CVPR*, pages 3858–3869, 2024.
- Danni Xu, Shaojing Fan, and Mohan Kankanhalli. Combating misinformation in the era of generative ai models. In *ACM MM*, pages 9291–9298, 2023.
- Zhipei Xu, Xuanyu Zhang, Runyi Li, Zecheng Tang, Qing Huang, and Jian Zhang. Fakeshield: Explainable image forgery detection and localization via multi-modal large language models. *arXiv preprint arXiv:2410.02761*, 2024.
- An Yang, Anfeng Li, Baosong Yang, Beichen Zhang, Binyuan Hui, Bo Zheng, Bowen Yu, Chang Gao, Chengen Huang, Chenxu Lv, et al. Qwen3 technical report. *arXiv preprint arXiv:2505.09388*, 2025.

- Ling Yang, Zhilong Zhang, Yang Song, Shenda Hong, Runsheng Xu, Yue Zhao, Wentao Zhang, Bin Cui, and Ming-Hsuan Yang. Diffusion models: A comprehensive survey of methods and applications. *ACM computing surveys*, 56(4):1–39, 2023.
- Chenshuang Zhang, Fei Pan, Junmo Kim, In So Kweon, and Chengzhi Mao. Imagenet-d: Benchmarking neural network robustness on diffusion synthetic object. In *CVPR*, pages 21752–21762, June 2024a.
- Jingyi Zhang, Jiaxing Huang, Sheng Jin, and Shijian Lu. Vision-language models for vision tasks: A survey. *IEEE Transactions on Pattern Analysis and Machine Intelligence*, 46(8):5625–5644, 2024b.
- Nan Zhong, Yiran Xu, Zhenxing Qian, and Xinpeng Zhang. Rich and poor texture contrast: A simple yet effective approach for ai-generated image detection. *CoRR*, 2023.
- Jun-Yan Zhu, Taesung Park, Phillip Isola, and Alexei A Efros. Unpaired image-to-image translation using cycle-consistent adversarial networks. In *ICCV*, pages 2223–2232, 2017.
- Mingjian Zhu, Hanting Chen, Qiangyu Yan, Xudong Huang, Guanyu Lin, Wei Li, Zhijun Tu, Hailin Hu, Jie Hu, and Yunhe Wang. Genimage: A million-scale benchmark for detecting ai-generated image. volume 36, pages 77771–77782, 2023.
- Giada Zingarini, Davide Cozzolino, Riccardo Corvi, Giovanni Poggi, and Luisa Verdoliva. M3dsynth: A dataset of medical 3d images with ai-generated local manipulations. In *ICASSP*, pages 13176–13180, 2024.

Appendix

A Visualization of Different τ

Our redefined pixel label M_τ is derived from the difference map using a tunable threshold τ . We visualize the results under different τ values in Fig. 11. Obviously, this threshold captures the spatial support of the edit at a controllable intensity level: a small τ emphasizes sensitivity to micro-edits, while larger τ emphasizes conservative, high-confidence changes. This thresholded construction decouples where an edit occurs (localization) from how strongly it manifests (intensity), enabling principled sweeps over τ to select operating points that best correlate with human judgments and downstream scenario use cases.

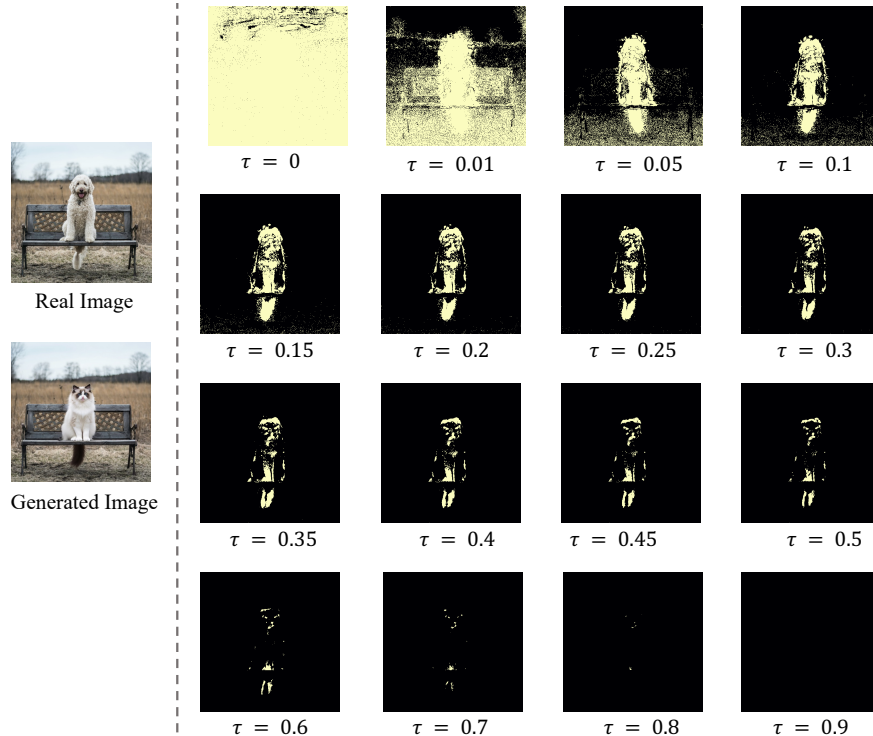


Figure 11 Visualization of pixel-level labels under different threshold values τ .

B Additional Implementation Details for Benchmark Construction

B.1 Image Generation

Qualitative Comparison of Generative Models. We conduct qualitative comparisons among several state-of-the-art open-source generative models, including Flux. 2 (Labs, 2025), and Qwen-Image (Wu et al., 2025). Examples are presented in Fig. 12. Among these models, *Qwen-Image VLMs consistently demonstrate higher perceptual fidelity and precise editing*, generating results that are nearly indistinguishable from real images in terms of texture realism, boundary coherence, and semantic consistency. Therefore, we adopt Qwen-Image VLMs as the generative model for training data generation.

Diverse and Practical Tampering Types. To ensure diversity, our pipeline integrates eight editing types. Examples of different manipulation types are shown in Fig. 13, and the type distribution is shown in Fig. 14a. Notably, some manipulations, such as object addition and background change, do not involve a mask during generation. Therefore, masks are not provided for these cases in the visualization images. Moreover, we emphasize the realistic and challenging intra-class replacement (e.g., apple \rightarrow another apple),



Figure 12 Visualization of tampered images generated by state-of-the-art open-source generative models.

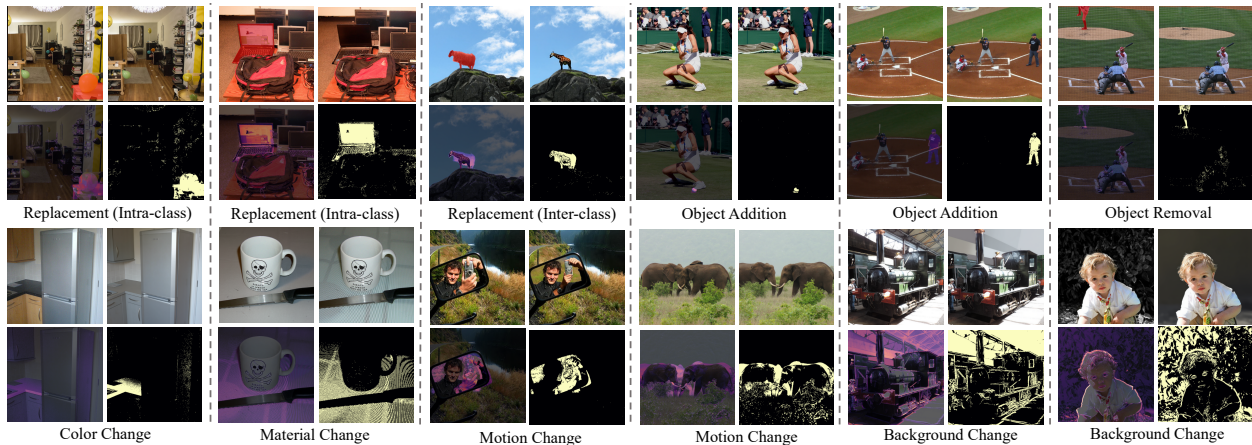
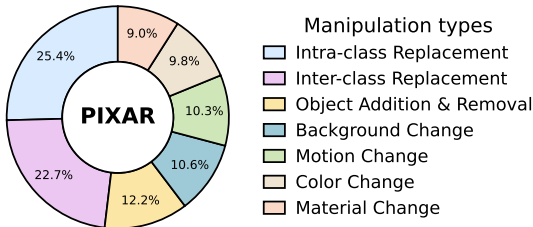
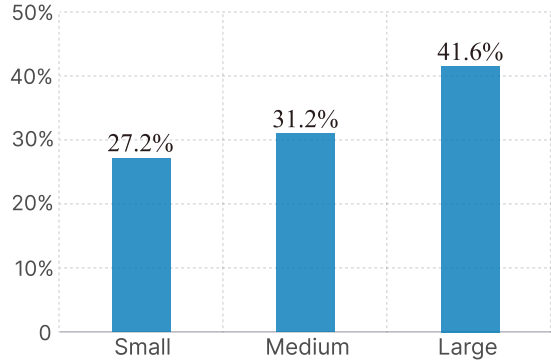


Figure 13 Visualization of various tampering types in PIXAR. For each type, from top-left to bottom-right, the images show: the original image (with the tampering mask shown in red, if applicable), the generated tampered image, the pixel-difference map overlaid on the generated image, and our pixel-level label.

which preserves critical attributes such as object pose, scale, and contextual consistency. These manipulations appear visually credible yet are inherently difficult to detect, thereby providing a more demanding evaluation setting. The type distribution of the training and test set is reported in Tab. 12 and Fig. 18 (ii).



(a) Tampered Type Distribution.



(b) Tampered Size Distribution.

Figure 14 Analysis of PIXAR Generated Images. (a) shows the distribution of different manipulation types. (b) shows the distribution of tampered sizes. We set the size categorization as: *small* indicates areas with fewer than 23000 pixels, *medium* indicates areas between 23000 and 50000 pixels, and *large* indicates areas with at least 50000 pixels.

Table 12 Dataset composition by manipulation type (including a multi-edit subset). Train total $N = 387,810$, Test total $N = 41,781$. **Mask** indicates whether a mask is used to guide the generation of tampered images. The three mask-conditioned training manipulations (intra-class replacement, inter-class replacement, and object removal; marked with \checkmark) form the LITE training subset, as referenced in Tab. 2.

Training set				Test set			
Manipulation	#	%	Mask	Manipulation	#	%	Mask
intra-class replacement	101206	26.10	\checkmark	intra-class replacement	5601	13.41	\times
inter-class replacement	89415	23.06	\checkmark	inter-class replacement	5965	14.27	\times
object removal	1059	0.27	\checkmark	object removal	5694	13.63	\times
object addition	39651	10.22	\times	object addition	4947	11.84	\times
color change	36687	9.46	\times	color change	4456	10.67	\times
motion change	38319	9.88	\times	motion change	4915	11.76	\times
material change	33981	8.76	\times	material change	3993	9.56	\times
background change	39851	10.28	\times	background change	4542	10.87	\times
multi-edit	7641	1.97	\times	multi-edit	1668	3.99	\times
Total	387810	100.00	-	Total	41781	100.00	-

Diverse Tampered Sizes and Complexities. To evaluate across a range of difficulty levels, we control two factors: *tampered size* and *tampered complexity*.

Tampered Size. Detection difficulty is strongly correlated with the extent of manipulation: small-scale edits induce subtle artifacts, whereas large-scale edits typically introduce substantial semantic changes. We define the tampered size as the *absolute* number of tampered pixels, and categorize the tampered size into *small* ($< 23,000$ pixels), *medium* ($[23,000, 50,000)$), and *large* ($\geq 50,000$), corresponding to approximately 7.5% and 16.5% of the average 640×480 image area in the COCO dataset. Representative examples are visualized in Fig. 4a, and the overall distribution is summarized in Fig. 14b.

Multi-Object Tampering. Beyond the prevalent single-object editing paradigm in existing datasets (Tab. 1), we introduce a *multi-object* tampering protocol that better reflects real-world forgery pipelines, which often compose multiple heterogeneous operations through iterative editing rather than a single isolated change. To increase compositional complexity, we construct a multi-edit subset where each image undergoes $K \in \{2, 3\}$ distinct manipulation types applied sequentially. Concretely, we perform the first edit on the source image and feed the intermediate output as the input to the subsequent editing pass. All hyper-parameters and prompts remain consistent with the single-object edit. For the multiple-edit setting, the training set contains 7,641 samples and the test set contains 1,668 samples. Within the test set, 459 image pairs undergo three edits.

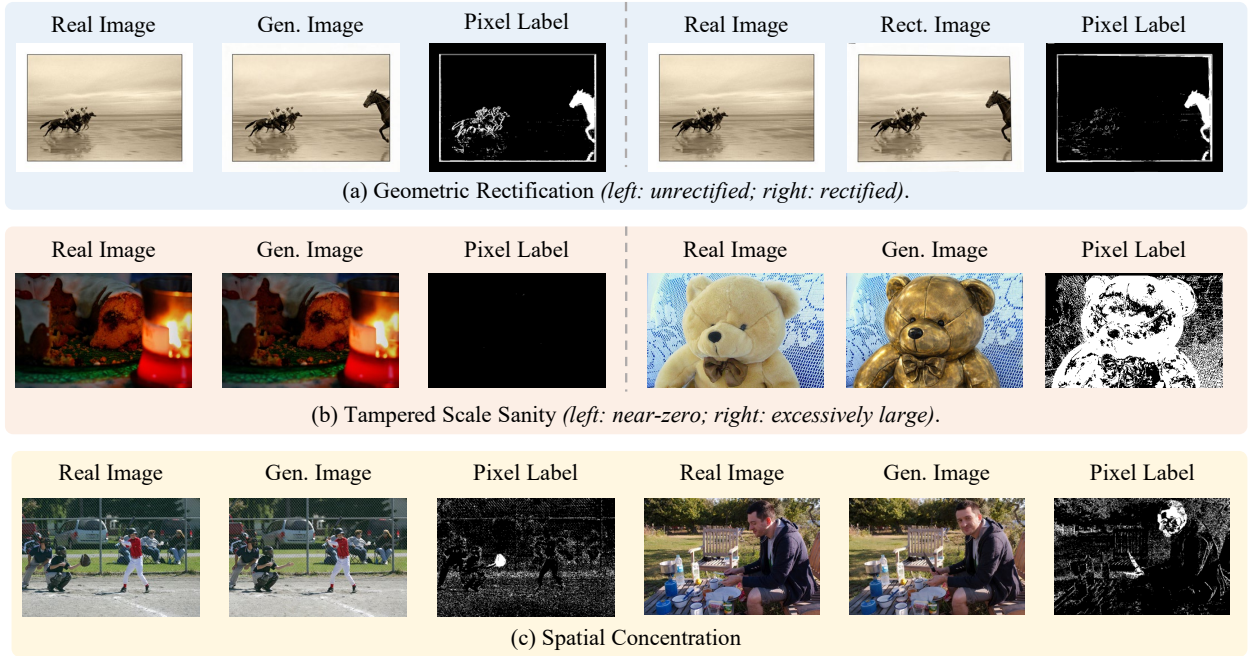


Figure 15 Tampering Effectiveness Checks and Label Reliability Checks. (a) Geometric Rectification; (b) Edit Magnitude Check; (c) Spatial Concentration

B.2 Tampering Effectiveness Checks

Global Rectification. We perform global rectification prior to computing the pixel difference map. Given $(I_{\text{orig}}, I_{\text{gen}})$, we first estimate a homography H that maps I_{gen} into the coordinate frame of I_{orig} using ORB feature matching (Rublee et al., 2011) and RANSAC (Fischler and Bolles, 1981). We then warp I_{gen} with H to obtain the aligned image $I_{\text{gen}}^{\text{align}}$ at the same resolution as I_{orig} . If homography estimation fails (e.g., insufficient matches), we fall back to using the unaligned I_{gen} .

Homography warping can create invalid pixels near image borders (e.g., black/undefined regions) and mild interpolation seams. To prevent these artifacts from being interpreted as tampering signals (see Fig. 15), we detect low-intensity pixels that are connected to the image border via flood fill, dilate the detected region to cover thin seams, and replace the detected boundary pixels with the corresponding pixels from I_{orig} . To avoid over-correction, we abort boundary filling if the detected boundary region exceeds a small area ratio (10% in our implementation).

Edit Magnitude Checks. We find that the tampered area is a strong indicator of generation failure (see Fig. 15 (b)). In particular: (i) *Near-zero tampering* (tampered size $\leq 2,480$) usually corresponds to negligible modifications, yielding pixel labels with little informative signal. (ii) *Excessively large tampering* (tampered size $\geq 184,500$) often indicates unintended global repainting, where the pixel label includes widespread differences beyond the target semantic region and introduces substantial noise. Therefore, we discard samples in these extreme regimes and retain only those whose tampered size falls within $[2,480, 184,500]$.

B.3 Image Fidelity Checks

Human Expert Review. To ensure high quality of PIXAR, we employ human experts to manually review the generated images and remove those that appear visually unrealistic. Only samples that received a realism score of at least 4 out of 5 were retained. Representative examples of filtered and retained samples in each manipulation are provided in Fig. 16. For each manipulation, we display four images: the first column shows two real images, and the second column shows their corresponding tampered images. Filtered samples with their corresponding real images are highlighted with an orange background, while retained samples are shown with a green background.



Figure 16 Visualization of samples filtered and retained by human evaluation. Images with an orange background indicate filtered samples, while those with a green background indicate retained images.

B.4 Label Reliability Checks

Pixel-Mask Overlap. In certain intra-class replacement cases (as illustrated in Fig. 7 of the main paper), the replaced and original objects exhibit highly similar colors and textures, making it challenging for pixel-level labels to accurately reflect true semantic tampering (i.e., the mask annotation). This results in discrepancies between pixel-level and semantic-level annotations.

To ensure label reliability, we filter out inconsistent cases. Specifically, we compute the overlap ratio between the tampered pixels and the input mask, and discard samples whose ratios fall below a predefined threshold, indicating substantial misalignment between pixel-level and semantic-level signals. Representative examples across ratios are visualized in Fig. 17. Obviously, as the overlap ratio increases, the consistency between pixel-level and semantic annotations improves notably. For instance, when the ratio is around 0.10, the labels fail to capture semantic information; at 0.15, they begin to reflect partial semantic content; and when the ratio exceeds 0.20, the pixel-level labels closely align with semantic annotations. Accordingly, we adopt a threshold of 0.2 to remove inconsistent samples, thereby maintaining the reliability of our labels.

Visualization of Spatial Concentration. Generation failures often yield pixel labels that are highly scattered across the image, appearing as unstructured noise rather than cohesive object boundaries (see Fig. 15(c)). While such dispersed labels can be semantically plausible, they are structurally uninformative. Motivated by this observation, we filter out spatially dispersed pixel label maps (e.g., background speckles) using two concentration scalars computed from the binary label map $M_\tau \in \{0, 1\}^{H \times W}$, inspired by dispersion in 2D binary patterns (Taubenbock et al., 2019) and local spatial association (Anselin, 1995).

Grid coverage ratio. To measure the global compactness of tampered pixels, we divide the binary mask M_τ into a uniform 10×10 grid cells. We then define r_{grid} as the smallest fraction of grid cells required to cover 80% of all tampered pixels. A smaller r_{grid} indicates that most tampered pixels are concentrated within a limited spatial region, whereas a larger value suggests a more dispersed distribution across the image.

Local density. Apart from global compactness, we also introduce a local density score r_{dens} to measure local spatial coherence among tampered pixels. Specifically, we apply a 7×7 mean filter to the binary mask M_τ and define r_{dens} as the median of the resulting filtered values. A high r_{dens} indicates that tampered pixels tend to be surrounded by other tampered pixels, suggesting a spatially contiguous or locally clustered region.

We classify each map as Concentrated or Diverse according to the fixed decision cases in Tab. 13, and discard Diverse samples. All hyperparameters are fixed throughout; we evaluated multiple candidates and selected the configuration that best matches visual judgments of cohesive vs. speckled labels.

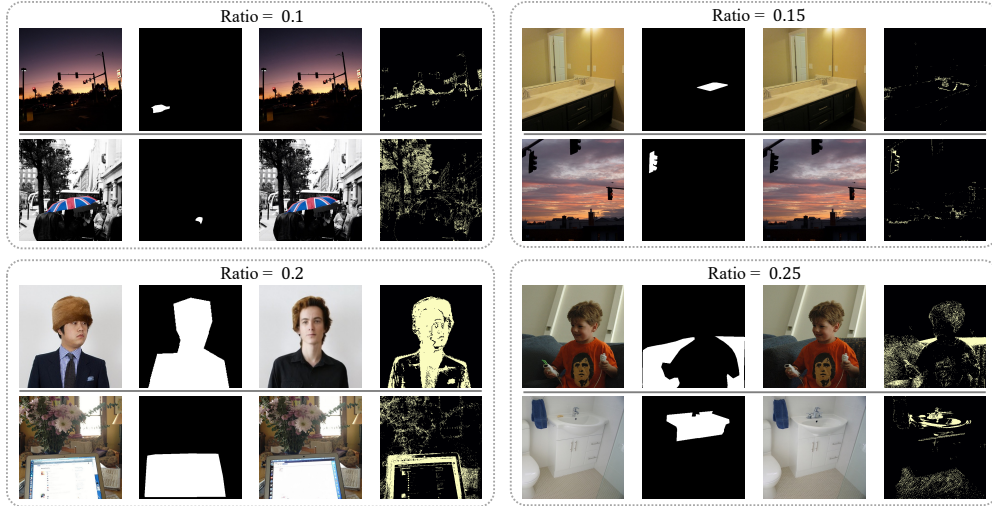


Figure 17 Visualization of examples under different overlap ratios. For each ratio, two examples are shown. For each example, from left to right: the original image, input mask, generated image, and our pixel label at $\tau = 0.05$.

Table 13 Spatial Concentration Check decision cases. Each row specifies one case for classifying a pixel label map using $(r_{\text{grid}}, r_{\text{dens}})$ and the tie-break score $r_{\text{grid}}(1 - r_{\text{dens}})$. Diverse samples are discarded in the pipeline.

r_{grid}	r_{dens}	$r_{\text{grid}}(1 - r_{\text{dens}})$	Label
$r_{\text{grid}} \leq 0.20$	—	—	Concentrated
$r_{\text{grid}} \geq 0.50$	—	—	Diverse
$0.20 < r_{\text{grid}} < 0.50$	$r_{\text{dens}} \geq 0.35$	—	Concentrated
$0.20 < r_{\text{grid}} < 0.50$	$r_{\text{dens}} \leq 0.25$	—	Diverse
$0.20 < r_{\text{grid}} < 0.50$	$0.25 < r_{\text{dens}} < 0.35$	$r_{\text{grid}}(1 - r_{\text{dens}}) \leq 0.25$	Concentrated
$0.20 < r_{\text{grid}} < 0.50$	$0.25 < r_{\text{dens}} < 0.35$	$r_{\text{grid}}(1 - r_{\text{dens}}) > 0.25$	Diverse

Table 14 Prompt templates for description construction. We deterministically map structured metadata to single-sentence tampering description. For multi-edit samples, we form a compositional explanation by concatenating the corresponding single-edit descriptions in the applied order.

Manipulation type	Template	Example
background change	The background was changed while keeping the foreground unchanged.	The background was changed while keeping the foreground unchanged.
object removal	The {orig} was removed from the image.	The car was removed from the image.
object addition	A {cat} was added to the image.	A bicycle was added to the image.
intra-class repl.	The {orig} was replaced with a different-looking {orig}.	The dog was replaced with a different-looking dog.
inter-class repl.	The {orig} was replaced with a {repl}.	The chair was replaced with a sofa.
color change	The color of the {cat} was changed.	The color of the shirt was changed.
motion change	The {cat} was edited to show a small motion change.	The person was edited to show a small motion change.
material change	The material appearance of the {cat} was changed.	The material appearance of the table was changed.
multi_edit	Concatenate the single-edit descriptions in the applied order.	The car was removed from the image. The background was changed while keeping the foreground unchanged.

B.5 Text Description

We follow a template-based instruction design to better leverage the fine-grained visual understanding of VLMs while keeping the conditioning signal controlled. Specifically, we generate a single-sentence edit description leveraging each tampered image’s structured metadata (Tab. 14). For multi-edit samples, we additionally provide a compositional textual explanation by concatenating the corresponding single-edit descriptions in the applied order. The instruction is intentionally minimal: it is restricted to the manipulation type, the affected category, and excludes non-semantic cues such as location, size, and image-quality descriptors. This

Table 15 Test set composition by generation model. Total $N = 41,781$.

Model	#	%
Qwen-Image (Wu et al., 2025)	8185	19.59
GPT-Image-1.5 (OpenAI, 2026)	7016	16.79
Flux.2 (Labs, 2025)	6651	15.92
Gemini 2.5 (Comanici et al., 2025b)	6636	15.88
Gemini 3 (DeepMind, 2025)	6716	16.07
Seedream 4.5 (Seedream et al., 2025)	6577	15.74
Total	41781	100.00

constrained design produces concise, semantically aligned edit descriptions that are easier for models to condition on and for humans to interpret.

C Balanced Test Data Construction

To ensure fair and comprehensive evaluation, we construct the test set with balanced distributions along three key dimensions: (i) tampered size, (ii) tampered object class, and (iii) tampering type. Furthermore, we incorporate diverse test samples generated by 6 state-of-the-art generative models to evaluate the generalization capabilities of detection models trained on our dataset (see Sec. 5.2). The final test set contains over 40K image pairs, each annotated with both pixel-level and semantic-level labels. All real images are sourced from the COCO validation split (val2017) Lin et al. (2014). The test set further includes samples produced by multiple state-of-the-art editing models; the per-model composition of the test set is summarized in Tab. 15.

Tampered Size Balance. We also ensure varying tampered-area size among tampered samples. We categorize the tampering scale into *small* ($< 23,000$ pixels), *medium* ($[23,000, 50,000)$), and *large* ($\geq 50,000$), corresponding to approximately 7.5% and 16.5% of the average 640×480 image area in the COCO dataset.

As shown in Fig. 18 (ii), the final distribution is approximately balanced to *Small:Medium:Large* = 4:3:3, providing a balanced composition while ensuring sufficient representation of small-scale manipulations, which are empirically more challenging to detect Pei et al. (2024).

Tampered Class Balance. COCO instance categories exhibit a naturally long-tailed distribution, with

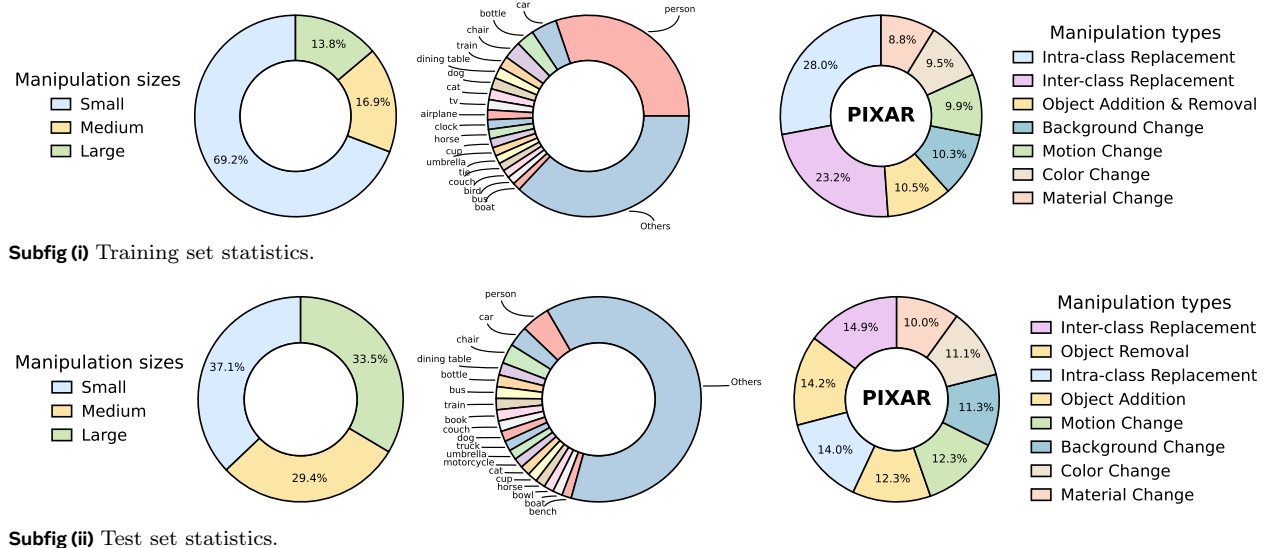


Figure 18 Dataset statistics in PIXAR. The upper and lower rows visualize the training and test partitions, respectively. In each row, from left to right, we report the distributions over (a) manipulation size, (b) manipulated object classes, and (c) manipulation types.

Table 16 Test set class distribution (single-edit subset). Total $N = 40,113$. We report per-class counts and percentages.

Top 25%			Top 50%			Top 75%			Bottom 25%		
Class	#	%	Class	#	%	Class	#	%	Class	#	%
person	1812	4.52	elephant	586	1.46	bird	464	1.16	hot dog	370	0.92
car	1308	3.26	tv	578	1.44	suitcase	464	1.16	sports ball	367	0.91
chair	1240	3.09	clock	572	1.43	sink	462	1.15	tie	362	0.90
dining table	784	1.95	potted plant	568	1.42	cell phone	459	1.14	remote	348	0.87
bottle	748	1.86	sheep	562	1.40	fire hydrant	456	1.14	donut	345	0.86
bus	740	1.84	cow	555	1.38	toilet	451	1.12	spoon	341	0.85
train	717	1.79	giraffe	543	1.35	vase	441	1.10	skis	331	0.83
book	707	1.76	traffic light	542	1.35	oven	438	1.09	orange	327	0.82
couch	669	1.67	pizza	518	1.29	carrot	437	1.09	microwave	321	0.80
dog	657	1.64	cake	515	1.28	wine glass	425	1.06	knife	319	0.80
truck	645	1.61	banana	511	1.27	parking meter	423	1.05	apple	317	0.79
umbrella	633	1.58	stop sign	509	1.27	sandwich	422	1.05	mouse	306	0.76
motorcycle	629	1.57	laptop	500	1.25	skateboard	420	1.05	baseball bat	278	0.69
cat	627	1.56	zebra	499	1.24	keyboard	408	1.02	baseball glove	275	0.69
cup	621	1.55	teddy bear	489	1.22	kite	401	1.00	snowboard	262	0.65
horse	620	1.55	bed	472	1.18	fork	389	0.97	frisbee	234	0.58
bowl	616	1.54	handbag	468	1.17	surfboard	388	0.97	toothbrush	229	0.57
boat	611	1.52	airplane	468	1.17	broccoli	387	0.96	scissors	219	0.55
bench	599	1.49	bear	468	1.17	backpack	377	0.94	hair drier	68	0.17
bicycle	592	1.48	refrigerator	464	1.16	tennis racket	375	0.93	toaster	45	0.11

several head classes (e.g., *person*, *car*) dominating the dataset. For example, in the original COCO distribution, the *person* category alone accounts for approximately 30%. To mitigate this imbalance, we downsample overrepresented categories to achieve a more balanced distribution across classes, as illustrated in Fig. 18 (ii). This adjustment ensures that the evaluation primarily reflects the detector’s generalization ability over diverse classes rather than its performance on a few dominant ones. We report the per-class counts and percentages of the test set in Tab. 16 (total $N = 40,113$).

Tampered Type Balance. The test set covers all eight manipulation types, consistent with the training set: intra-class replacement, inter-class replacement, object removal, object addition, color change, motion change, material change, and background change. We empirically observe that inter-class replacement and object removal exhibit lower generation success rates due to complex context blending. For example, the generation success rate of inter-class replacement is only about one-fifth that of intra-class replacement after VLM-based scoring and is further reduced following human evaluation, as illustrated in Sec. 3.2 of the main paper. To compensate, we intentionally emphasize these low-success-rate types during data generation. The resulting distribution across manipulation types is summarized in Fig. 18 (ii).

D Pixel Localization Metrics

Following the evaluation protocol in our benchmark, we comprehensively assess the pixel-level localization performance of a detector using five complementary metrics: **Recall**, **F1-Score**, **AUC**, **g-IoU**, and **IoU**. These metrics jointly measure detection sensitivity, precision–recall trade-off, overall discrimination capability, and spatial alignment quality between predicted and ground-truth tampered regions. Given a pair of real and tampered images ($I_{\text{orig}}, I_{\text{gen}}$), the model produces pixel-level prediction, while the benchmark provides the pixel label M_T . For evaluation, we compute true positives (TP), false positives (FP), false negatives (FN), and true negatives (TN) at the pixel level.

(1) Recall. Pixel-level recall quantifies the fraction of correctly detected tampered pixels among all truly tampered pixels:

$$\text{Recall} = \frac{\text{TP}}{\text{TP} + \text{FN}}, \quad (9)$$

where TP and FN denote true positives and false negatives, respectively.

(2) F1-Score. Given precision $\text{Prec} = \frac{\text{TP}}{\text{TP} + \text{FP}}$, the F1-score provides a harmonic balance between precision and recall:

$$\text{F1} = \frac{2 \times \text{Prec} \times \text{Recall}}{\text{Prec} + \text{Recall}} = \frac{2 \times \text{TP}}{2 \times \text{TP} + \text{FP} + \text{FN}}. \quad (10)$$

(3) AUC. The Area Under the ROC Curve (AUC) is obtained by sweeping the decision threshold over $[0, 1]$ to compute the true positive rate (TPR) and false positive rate (FPR):

$$\text{AUC} = \int_0^1 \text{TPR}(\text{FPR}) d(\text{FPR}), \quad (11)$$

where $\text{TPR} = \frac{\text{TP}}{\text{TP} + \text{FN}}$ and $\text{FPR} = \frac{\text{FP}}{\text{FP} + \text{TN}}$. This metric measures the overall discriminability of the detector independent of a specific threshold.

(4) IoU. The conventional intersection-over-union (IoU) is defined as

$$\text{IoU} = \frac{\text{TP}}{\text{TP} + \text{FP} + \text{FN}}. \quad (12)$$

IoU directly measures the spatial overlap between predicted and ground-truth tampered pixels, providing an interpretable indicator of localization accuracy.

(5) g-IoU. The global IoU (g-IoU) in our implementation is the mean IoU across all tampered samples:

$$\text{g-IoU} = \frac{1}{N} \sum_{i=1}^N \frac{|\widehat{\mathbf{M}}_i \cap \mathbf{M}_{\tau,i}|}{|\widehat{\mathbf{M}}_i \cup \mathbf{M}_{\tau,i}| + \varepsilon}, \quad (13)$$

where $\widehat{\mathbf{M}}_i$ and $\mathbf{M}_{\tau,i}$ denote the predicted and pixel labels of sample i , and ε is a small constant to avoid division by zero.